JOM Journal of Optical Microsystems

RESEARCH PAPER

# Compact scattering-based light sheet microscopy probe using a custom miniature objective lens

**Jingwei Zhao**,[a] **Yongjun Kim**,[b] **Momoka Sugimura**,[a] **Kenneth Marcelino**,[a]
**Rafael Romero**,[b] **Brooke Liang**,[c] **Michelle Khan**,[d] **Eric Yang**,[c] and
**Dongkyun Kang**[a,b,*]
[a]University of Arizona, James C. Wyant College of Optical Sciences, Tucson, Arizona, United States
[b]University of Arizona, Department of Biomedical Engineering, Tucson, Arizona, United States
[c]Stanford University School of Medicine, Department of Pathology, Stanford, California, United States
[d]Stanford University School of Medicine, Department of Obstetrics and Gynecology, Stanford, California, United States

---

**ABSTRACT.** We have developed a compact scattering-based light sheet microscopy (sLSM) probe capable of imaging unstained tissues with cellular resolution. In the compact sLSM probe, a custom miniature objective lens was developed to achieve a high lateral resolution, large field of view (FOV), and small field curvature. The measured resolution of the custom objective was 1.65 to 1.97 $\mu$m across the FOV of $\pm 1.0$ mm. The compact probe had dimensions of 4 cm in width and height and 10 cm in length. The compact sLSM probe achieved an axial resolution better than 5.6 $\mu$m over a depth range of 206.2 $\mu$m and a lateral resolution of 1.9 $\mu$m. Preliminary results showed that the compact sLSM probe could visualize cellular details of fixed human anal epithelial tissues in a similar manner to a bench light sheet microscopy device using off-the-shelf objective lenses.

[DOI: 10.1117/1.JOM.4.3.034501]

**Keywords:** light sheet microscopy; compact microscope; unstained tissue imaging; miniature objective lens; custom objective lens; intrinsic scattering

Paper 24010G received Mar. 12, 2024; revised Jul. 10, 2024; accepted Jul. 12, 2024; published Aug. 6, 2024.

---

## 1 Introduction

*In vivo* microscopy enables direct visualization of certain cellular morphologic changes associated with diseases in human tissues without removing the tissue from the patient.[1] Reflectance confocal microscopy (RCM) and optical coherence tomography (OCT) are two of the *in vivo* microscopy technologies translated into clinically viable medical devices.[2,3] However, a common challenge in *in vivo* microscopy is the difficulty of achieving both high resolution and large field of view (FOV) simultaneously. For instance, commercial RCM devices for dermatology applications offer high lateral (1 $\mu$m) and axial (5 $\mu$m) resolutions.[4] However, *en face* images provided by RCM typically have a small FOV of 500 to 750 $\mu$m,[5,6] making it challenging to examine wide areas of the tissue. Conversely, OCT can provide cross-sectional images of the tissue with a larger FOV (>1 mm) but with a lateral resolution of 10 to 20 $\mu$m, which is more suitable for visualizing architectural features than cellular and sub-cellular details.[6,7] Recently, high-resolution OCT achieved both high resolution and large FOV,[8,9] but the broadband coherent light source used in high-resolution OCT could increase the cost of the device.

Light sheet microscopy (LSM) is a microscopy approach that has been mainly used for imaging tissues or small animals in basic life science research.[10–12] In LSM, the illumination

---

*Address all correspondence to Dongkyun Kang, dkkang@arizona.edu

and detection paths are separated, with the illumination confined to a thin plane that is conjugate to the detection focal plane. The thin plane illumination enables imaging of a thin section inside a thick tissue. LSM has been mainly used for fluorescence imaging using either exogenous contrast agents or intrinsic autofluorescence signal.[12–14] In most LSM devices, high-NA objective lenses are used to achieve sub-cellular lateral resolution (<1 $\mu$m).

If intrinsic scattering signals can be used to generate image contrast in LSM, as in RCM and OCT, it might be possible to adapt LSM for imaging freshly excised human tissues *ex vivo* or human patients *in vivo*. If the requirements for the lateral and axial resolution of LSM could be relaxed to the resolution shown useful for imaging cellular structures in *in vivo* microscopy of human tissues (lateral resolution = 1 to 2 $\mu$m, axial resolution = ~5 $\mu$m), an objective lens with a moderate NA (~0.3) could be used, which in turn could provide a larger FOV that is comparable to the typical FOV of OCT.

We previously adapted LSM for imaging cellular structures of unstained tissues using intrinsic scattering contrast, which we termed scattering-based LSM or scattering-based light sheet microscopy (sLSM). In bench sLSM setups, we demonstrated the capability of imaging unstained animal or human tissue *ex vivo* with a high resolution (lateral resolution = 1.0 to 1.8 $\mu$m, axial resolution = 5.0 to 6.7 $\mu$m) over a relatively large FOV (1.5 to 2.5 mm).[15–17] We also conducted a pilot study imaging fresh human anal biopsies *ex vivo* with a bench sLSM setup.[18] The sLSM images clearly showed the morphological changes associated with anal squamous intraepithelial lesions in a similar manner to hematoxylin and eosin (H&E)-stained histologic images. The next important step is to evaluate the feasibility of developing a compact sLSM probe.

In this paper, we report the design and development of a compact sLSM probe. Instead of using an off-the-shelf objective lens, we developed a custom miniature objective lens to achieve high resolution, large FOV, and small field curvature. The optical performance of the custom objective lens and the compact sLSM probe was tested with standard and custom resolution targets. Tissue imaging performance was tested by imaging formalin-fixed human anal epithelial tissues *ex vivo*.

## 2 Methods

### 2.1 Compact sLSM Probe Design

Figure 1 shows a schematic of the compact sLSM probe. In the illumination path, a laser (B073H21NJP, Sunshine electronics; wavelength = 638 nm; output power = 1.0 W) was used as the light source. In our previous work investigating the optimal wavelength for sLSM, we found that a wavelength around 600 nm provides a good balance between the imaging depth and resolution. Therefore, the wavelength of 638 nm was used in the compact sLSM probe.[16] Light from the laser was coupled into a multimode fiber (02-511, Edmund optics; fiber diameter = 2.0 mm; core diameter = 1.96 mm; NA = 0.5). In between the laser and fiber, a rotating diffuser (DG10-1500, Thorlabs; grit = 1500; rotation speed = 600 rpm) was used to

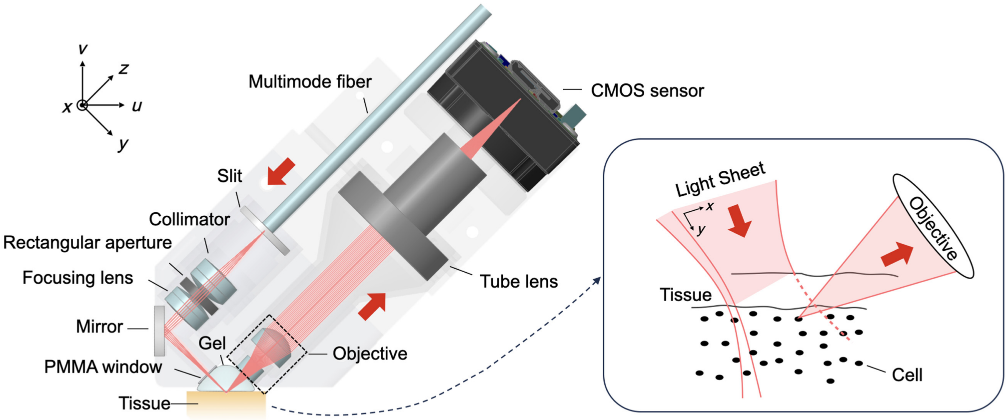

Fig. 1 Schematic of the compact sLSM probe.

reduce the speckle noise. An illumination slit (2-2.5-3+HS+M-0.5, National Aperture; width $= 2.5~\mu$m; length = 3.0 mm) was used to shape the spatially incoherent light from the fiber into a narrow line, which was imaged on the tissue to generate the light sheet illumination.[17] The light passing through the slit was collimated by an achromatic doublet (49-926, Edmund optics; $f = 15$ mm). The collimated light passed through a three-dimensional (3D)-printed rectangular aperture and focused by another achromatic doublet (49-927, Edmund optics; $f = 22.5$ mm). The illumination beam was folded by a dielectric mirror (87-367, Edmund optics; reflectivity $> 99\%$) and transmitted through a plastic imaging window [material = polymethyl methacrylate (PMMA); thickness $= 250~\mu$m; flat] to form a light sheet on the tissue. An immersion medium (GenTeal Tears Gel, Alcon; refractive index = 1.34) was used to fill the space between the plastic imaging window and the tissue.

In the detection path, scattered light from the tissue was collected by a custom objective lens ($f = 14.9$ mm; NA = 0.25) and focused by a tube lens (66-896, Edmund optics; multi-element micro video lens; $f = 35$ mm; F/2) onto a monochromatic CMOS sensor (daA3840-45um, Basler; $3{,}840 \times 2{,}160$ pixels; pixel size $= 2.0~\mu$m; imaging speed = 45 fps). The distal end of the bi-concave lens was in contact with the immersion medium. The detection optics had a magnification of 2.35, resulting in the pixel size of $0.85~\mu$m and the FOV of $3.26~\text{mm} \times 1.84$ mm on the tissue $xy$-plane.

Mechanical holders were custom designed and fabricated using a 3D printer (Form 3+, Formlabs) and biocompatible material (biomed black resin, Formlabs). Most of the optical elements were passively aligned using tight fit with the mechanical holders to ensure concentricity, whereas some optical components were actively aligned.

### 2.2 Custom Objective Lens Design

Previously, several custom objective lenses were successfully developed for microscopic imaging of tissues. These objective lenses achieved a high NA (0.5 to 1.0) while either reducing the overall lens size for endoscopy applications[19–21] or increasing the FOV for large-area imaging.[22] However, these lenses needed to use multiple elements (>5) in order to achieve a high NA. In sLSM, the use of a single wavelength and small NA (<0.3) could make it possible to use fewer elements for the custom objective lens. In the compact sLSM probe, we designed a custom objective lens composed of two elements, an aspheric convex lens (material = PMMA) and an aspheric bi-concave lens (material = PMMA) as shown in Fig. 2(a). The custom objective lens was designed using OpticsStudio (Zemax).

The aspheric convex lens had an aspheric surface on the proximal side (farther from the tissue) and a nearly flat surface on the distal side (closer to the tissue). The lens stop was located on the proximal side. The bi-concave lens had an aspheric surface on the proximal side and a spherical surface on the distal side. The two aspheric lenses were fabricated by diamond turning. The convex lens had the clear aperture of 7.4 mm in diameter and center thickness of 5.0 mm. The bi-concave lens had the clear aperture of 4.6 mm in diameter and center thickness of 2.9 mm. The distance between the two lens elements was designed as 3.0 mm. During the alignment procedure, the distance between the two lenses was actively adjusted to minimize the full-width-half-maximum (FWHM) of the measured point-spread function (PSF). A stainless-steel washer (thickness = 0.05 mm, outer diameter = 4.7 mm, inner diameter = 3.2 mm) was placed on

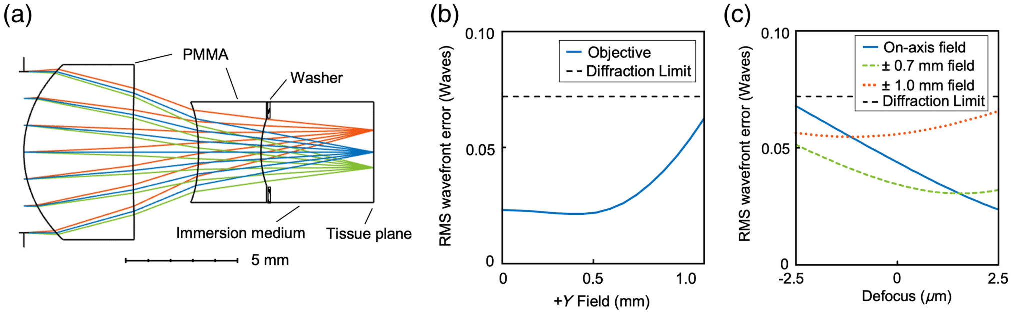

**Fig. 2** (a) Schematic of the custom objective lens, (b) wavefront error performance as a function of field, and (c) wavefront error performance as a function of defocus.

the distal flange of the bi-convex lens to block stray light. During the optimization process, both the working distance and the diameter of the bi-concave lens were regulated to prevent mechanical interference between the lens and tissue when the objective lens is angled at 45 deg relative to the tissue surface.

The effective focal length and NA of the objective lens were 14.9 mm and 0.25, respectively. The theoretical resolution at 638 nm was 1.32 $\mu$m. The lens was designed to have a diffraction-limited FOV of $\pm 1.0$ mm in the tissue space, as shown in the root-mean-square (RMS) wavefront error plot as a function of field [Fig. 2(b)]. In our previous sLSM work imaging anal tissues with water-immersion objective lenses and immersion medium with the index of 1.34, sLSM was able to visualize nuclear features over the 100 to 200 $\mu$m thickness of anal epithelial tissues.[23] We evaluated the RMS wavefront error of the custom objective lens when imaging epithelial tissues with an index higher than 1.34 at the detection angle of 45 deg. For an assumed tissue index of 1.357,[24] the custom objective lens is expected to have a diffraction-limited performance over the imaging depth of 200 $\mu$m. For a tissue index of 1.393,[25] the custom objective lens is expected to have a diffraction-limited performance over the depth of 100 $\mu$m, sufficient for evaluating nuclear morphologic differences between normal/low-grade lesions and high-grade lesions. The field curvature of the lens was controlled to have diffraction-limited performance within the defocus range of $\pm 2.5$ $\mu$m, corresponding to the theoretical thickness of the light sheet illumination, as shown in Fig. 2(c). A Monte-Carlo tolerance analysis was conducted on the objective lens based on the lens manufacturing tolerances.[26] The tolerance analysis showed that more than 72% of the objective lenses would provide diffraction-limited performance.

## 2.3 Light Sheet Thickness Simulation

For sLSM imaging, it is critical to maintain a thin light sheet thickness over a large depth range (along the $y$-axis in Fig. 1). This can be achieved by using a small NA for illumination. However, with such a small illumination NA, a highly scattering object in the tissue can cast shadow on cellular structures underneath it. This shadow effect manifests as dark vertical stripes in sLSM images.[27] Previously, we demonstrated that a rectangular aperture in the illumination path with an aspect ratio greater than 3 can effectively reduce the shadow artifacts while maintaining a thin light sheet thickness.[17] In the compact sLSM probe, the aperture length along the $x$-axis and width along the $y$-axis were set to 9.0 and 2.9 mm, respectively, to provide the illumination NA of 0.2 along the $x$-axis and 0.06 along the $z$-axis (after 90 deg reflection by the fold mirror). This aperture arrangement resulted in hourglass-shape light sheet illumination with a theoretical thickness of 5.0 $\mu$m and depth of focus (DOF) of 206.2 $\mu$m.

The choice of lenses in the illumination optics was initially based on first-order geometric optics. Therefore, the illumination performance degradation caused by aberrations was not initially considered. Given that the PMMA window and immersion medium would introduce aberrations, it was necessary to ensure the focusing light sheet meets the target thickness requirement. Due to the larger NA along the $x$-axis and smaller NA along the $z$-axis, aberrations were mainly expected along the $x$-axis, as shown in the simulated Huygens PSF [Fig. 3(a)]. The light sheet illumination, determined by the convolution between the PSF and image of the slit (longer along the $x$-axis), therefore maintains a narrow thickness, as shown in Fig. 3(a). We evaluated the light sheet thickness for different fields (along the $x$-axis) and different defocus locations (along the $y$-axis) to ensure the light sheet thickness was consistently small across the entire imaging FOV and depth range. The light sheet thickness for different fields ($x = 0$ and $\pm 1.0$ mm) and defocus locations ($y = 0$ and $\pm 103.1$ $\mu$m) was simulated using the extended diffraction image analysis function in OpticsStudio, which considered both diffraction and aberration effects of the illumination optics. As shown in Fig. 3(b), the theoretical light sheet thickness was maintained small, ~5.0 $\mu$m, even though aberrations were present along the $x$-axis.

## 2.4 Custom Objective Lens Performance Test

Optical performance of the objective lens was evaluated by imaging a UASF resolution target and a custom multi-pinhole target. The UASF resolution target image was used to identify the smallest resolvable line period. The image of the custom multi-pinhole target was used to measure the FWHM of the PSF across the entire FOV. The custom multi-pinhole target had pinholes periodically spaced along horizontal and vertical directions (pinhole diameter $= 0.67$ $\mu$m;

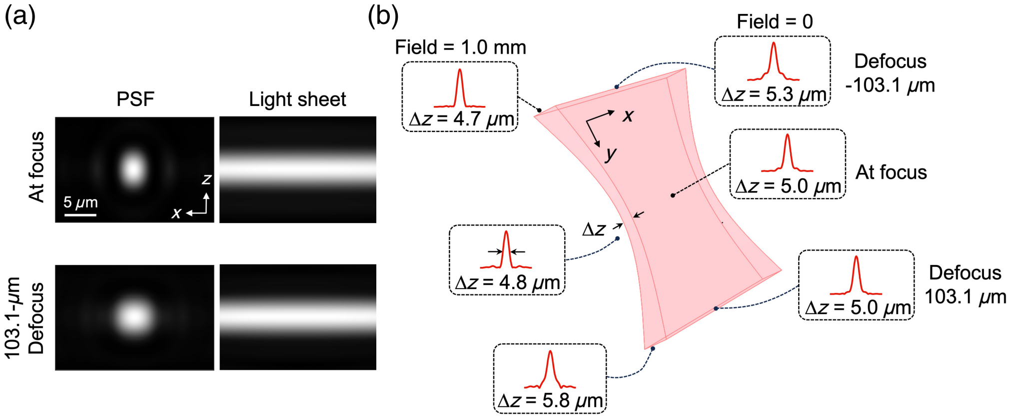

**Fig. 3** (a) Simulated Huygens PSFs and light sheet illumination for the on-axis field at the focus and at 103.1-μm defocus and (b) light sheet thickness for different fields and defocus locations.

period = 20 μm). The multi-pinhole target was fabricated by etching the pinhole pattern on a glass substrate (thickness = 1.5 mm) deposited with reflective chrome coating. We conducted a simulation of the effect of the pinhole size by convolving the theoretical PSF of the objective lens with the pinhole geometry and calculating the FWHM of the convolved profile. The simulation results showed that only a small amount of measurement error (5%) was expected when measuring the expected resolution of 1.32 μm. The period of the pinhole pattern, 20 μm, was set significantly larger than the pinhole diameter so that the image of each pinhole does not affect the image of neighboring pinholes.

In order to evaluate the performance of the objective lens alone, the detection optics were assembled and mounted vertically facing downward. The USAF resolution target or the multi-pinhole target was placed horizontally under the objective lens and was trans-illuminated from below the target. Light transmitted through the target was collected by the objective lens and imaged by the tube lens onto the CMOS sensor.

### 2.5 Probe Performance Test

The axial and lateral resolution of the sLSM probe was measured simultaneously by imaging a custom resolution target with a periodic line pattern (line width = 0.5 μm; period = 30 μm) we previously developed.[16] The line pattern was made on a chrome-coated glass substrate (thickness = 1 mm) by photolithography and etching. The target was placed horizontally with the reflective lines parallel to the $u$-axis and facing upward. Only a small portion of each line was illuminated by the light sheet, with the illumination width determined by the thickness of the light sheet. The lines reflected the illumination light toward the detection optics, producing an image that showed multiple partial lines. In the sLSM image of the line pattern, the FWHM of the line height along the $y$-axis was measured as the axial resolution of sLSM. The FWHM of the line width was measured as the line-spread function (LSF) or the lateral resolution of the detection optics. Therefore, both the lateral and axial resolution was measured from a single sLSM image of the line pattern at a given depth. The resolution target was translated along the $v$-axis with a step size of 10 μm to measure the resolution at different imaging depths. The exposure time of the CMOS sensor was adaptively adjusted to avoid the signal saturation. Index-matching gel (GenTeal Tears Gel, Alcon) was placed between the resolution target and the probe as an immersion medium.

Tissue imaging performance was tested by imaging formalin-fixed human anal tissues *ex vivo*. The sLSM images acquired by the compact probe were compared with the images previously acquired with the bench sLSM device[17] using off-the-shelf objective lenses (N10XW-PF, Nikon; $f = 20$ mm; NA = 0.3; water immersion) and H&E-stained histologic images. The epithelial side of the tissue was placed upward. The index-matching gel was placed between the tissue and probe. The protocol for imaging formalin-fixed human anal tissues *ex vivo* was reviewed and approved by the Stanford University and University of Arizona Internal Review Boards (IRBs). Informed consent was waived by the IRBs for this study imaging discarded fixed tissues. Cellular features visualized in sLSM images were analyzed in comparison with the features shown in the corresponding histologic images by an expert pathologist (EY).

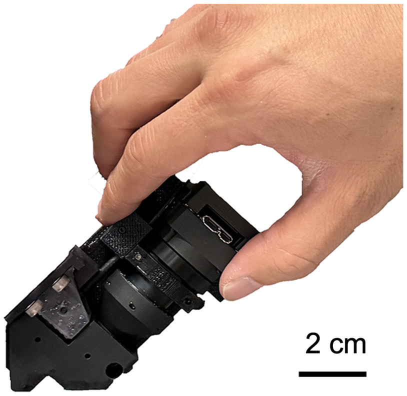

**Fig. 4** Photo of the sLSM probe.

# 3 Results

## 3.1 Compact sLSM Probe

A photograph of the compact sLSM probe is shown in Fig. 4. Overall dimensions of the prototype were 4 cm in height and width and 10 cm in length. The illumination power on the tissue was 0.14 mW. The exposure time was set at ∼0.5 ms, resulting in a real-time imaging speed with a frame rate of 45 fps, which is the highest frame rate the CMOS sensor supported. The material cost of the compact sLSM probe was low, <\$2000. The unit price of the custom objective lens was relatively high, \$1200, due to the cost associated with diamond turning and anti-reflection coating. The objective lens cost can be reduced significantly by using injection molding in the future.

## 3.2 Custom Objective Lens Performance

A representative image of the USAF resolution target is shown in Fig. 5(a). The smallest line pattern resolvable by the custom objective lens was group 9, element 1 (linewidth = 0.97 $\mu$m)

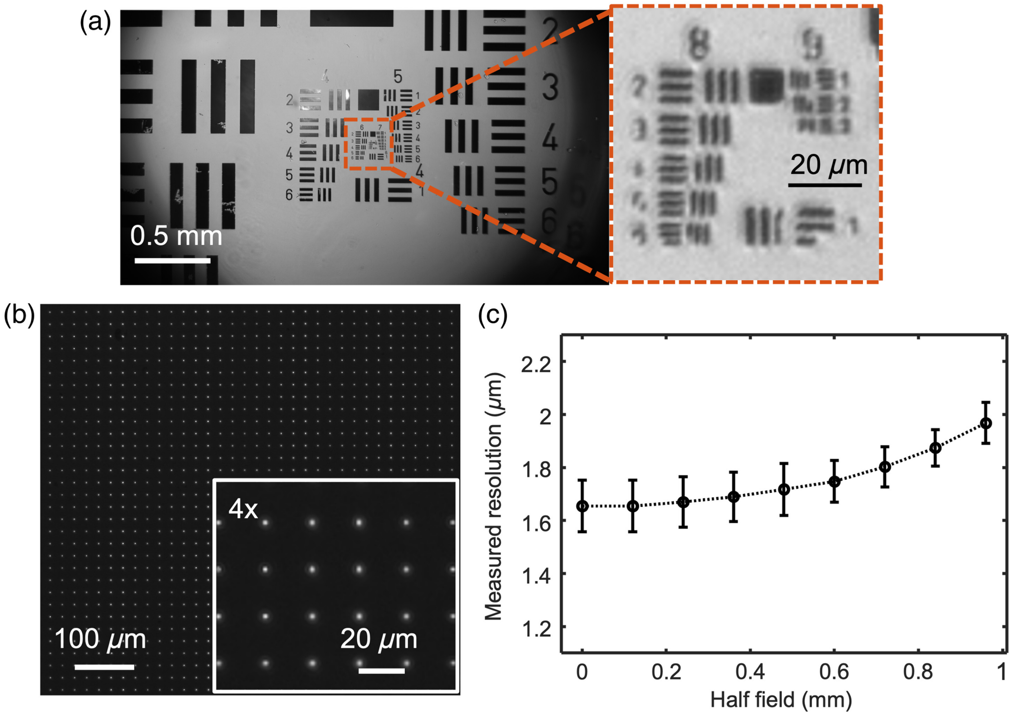

**Fig. 5** (a) USAF target image, (b) custom multi-pinhole target image, and (c) measured resolution as a function of field of the custom objective lens.

along both the horizontal and vertical directions, as shown in the inset of Fig. 5(a). However, the USAF image exhibited obvious side lobes surrounding the line pattern, indicating the presence of aberrations. A representative image of the custom multi-pinhole target is shown in Fig. 5(b). The measured PSF FWHM of the custom objective lens as a function of field [Fig. 5(c)] shows that the custom objective lens provides the resolution of 1.65 to 1.97 $\mu$m across the FOV of ±1.0 mm.

### 3.3 Probe Resolution Measurement

Figure 6(a) shows a representative image of the custom line pattern target captured by the compact sLSM probe. The measured LSF FWHM, also the measured lateral resolution, was $1.90 \pm 0.07$ $\mu$m over the theoretical illumination DOF of 206.2 $\mu$m. The axial resolution at the center of the imaging depth range was measured to be 5.2 $\mu$m. Within the theoretical illumination DOF of 206.2 $\mu$m, the light sheet thickness, also the axial resolution, was smaller than 5.6 $\mu$m.

### 3.4 Tissue Imaging Performance

Figure 7 shows representative sLSM and histologic images of fixed normal anal squamous mucosa. The image acquired by the compact sLSM probe [Fig. 7(a)] visualizes tissue details over a width of 2 mm. The epithelium and stroma are clearly delineated. A magnified view of the same image [Fig. 7(b)] visualizes a honeycomb pattern of squamous epithelial cells with hypo-reflective nuclei (arrows) and hyper-reflective cytoplasm and cell membranes, in a similar manner to the image obtained with the bench sLSM device [Fig. 7(c)] and with a similar nuclear size and spacing to the histologic image [Fig. 7(d)].

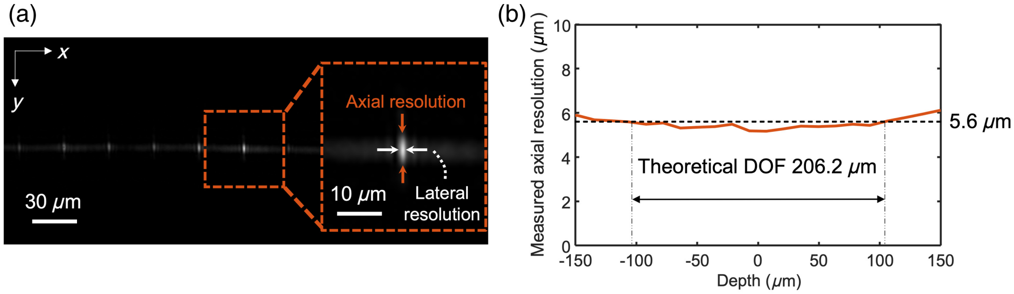

**Fig. 6** (a) Custom resolution target image and (b) measured axial resolution as a function of depth.

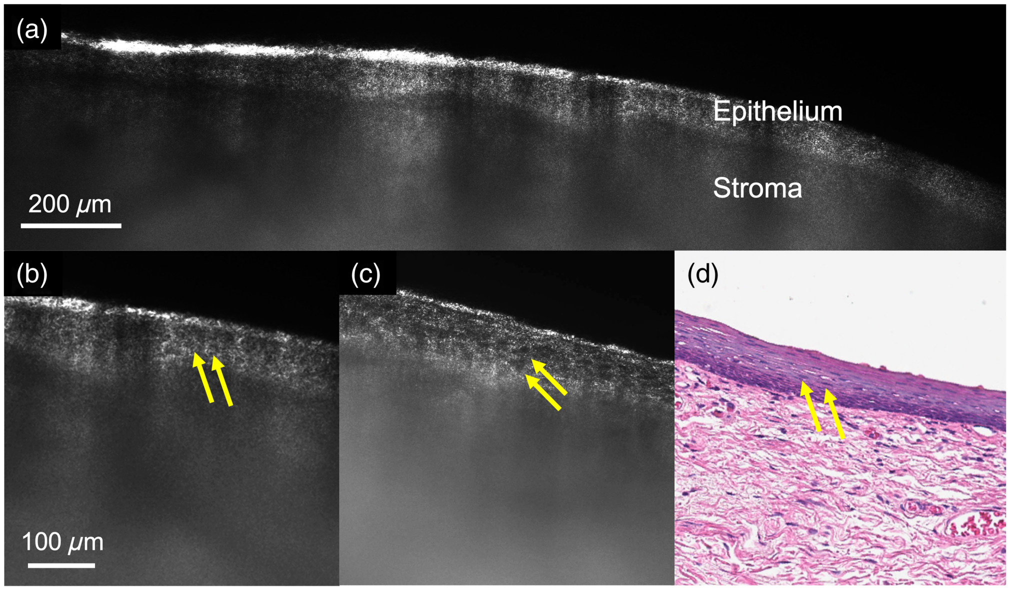

**Fig. 7** sLSM images of normal anal squamous mucosa obtained with (a, b) the compact sLSM probe and (c) bench sLSM device, and (d) histologic image of the same tissue. Arrows, nuclei.

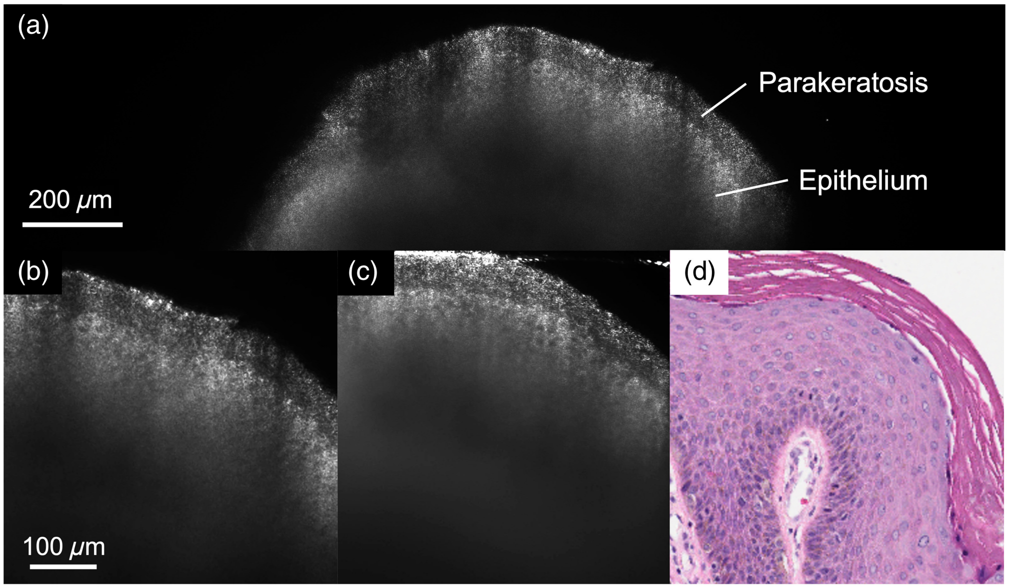

**Fig. 8** sLSM images of LSIL obtained with (a, b) the compact sLSM probe and (c) bench sLSM device, and (d) histologic image of the same tissue.

Figure 8 shows representative sLSM and histologic images of fixed low-grade squamous intraepithelial lesion (LSIL). The image obtained with the compact sLSM probe [Fig. 8(a)] clearly distinguishes the layer of parakeratosis from the underlying epithelium, which is thickened compared to normal squamous epithelium. The higher-magnification view of the compact sLSM probe image [Fig. 8(b)] shows that the honeycomb pattern of the squamous epithelial cells is still retained but the cellular features have more variability in size and shape than normal squamous epithelium. A similar trend is shown in the image obtained with the bench sLSM device [Fig. 8(c)] and the histologic image [Fig. 8(d)].

Figure 9 shows representative sLSM and histologic images of fixed high-grade squamous intraepithelial lesion (HSIL). A large-area sLSM image obtained with the compact sLSM probe [Fig. 9(a)] shows the lack of clear distinction between the epithelium and stroma. The increased epithelial thickness and stronger scattering in HSIL might have degraded the resolution at the

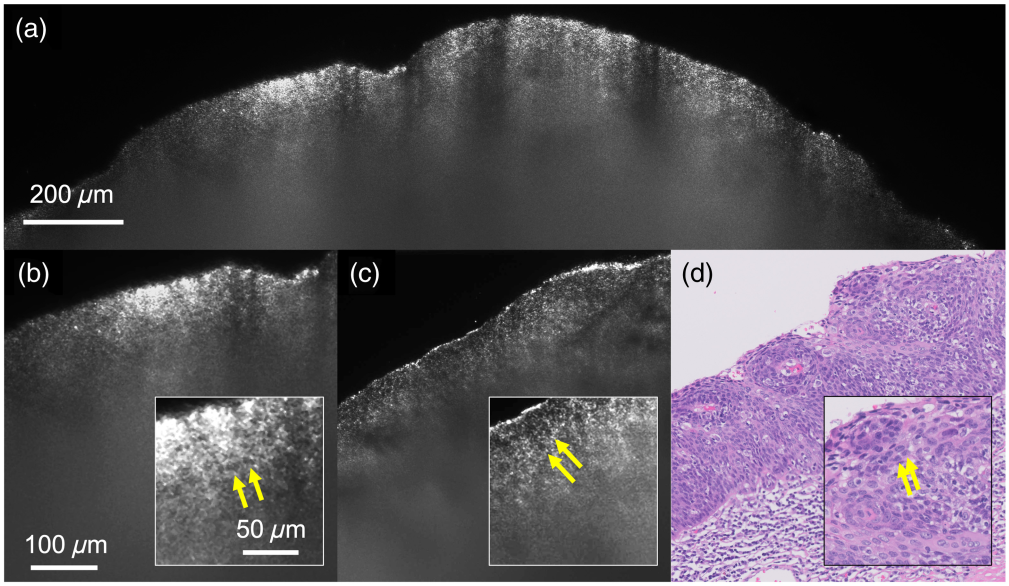

**Fig. 9** sLSM images of HSIL obtained with (a, b) the compact sLSM probe and (c) bench sLSM device, and (d) histologic image of the same tissue. Arrows, nuclei.

base of the epithelium more in HSIL than in normal squamous epithelium, making the epithelium-to-stroma interface less distinctive. A higher-magnification view [Fig. 9(b)] and its inset visualize dense and irregular arrangement of small hypo-reflective nuclei (arrows) with a varying size and shape. The trend of crowded nuclei is also shown in the image obtained with the bench sLSM device [Fig. 9(c)] and the histologic image [Fig. 9(d)].

## 4 Discussion

In this paper, we presented the development of a compact sLSM probe that can visualize cellular details of unstained tissues just using the intrinsic scattering contrast. We designed a custom miniature objective lens to achieve the NA of 0.25 with a diffraction-limited FOV of ±1.0 mm. The field curvature of the custom objective lens was made small to ensure the detection focal plane coincided with the illumination plane within the target FOV. The compact probe achieved the lateral resolution of $1.90 \pm 0.07$ $\mu$m and axial resolution better than 5.6 $\mu$m over a depth range of 206.2 $\mu$m. The illumination power on the tissue of 0.14 mW allowed for a short exposure time even when imaging fixed human anal tissues. Preliminary results showed that the compact sLSM probe was able to visualize cellular features in formalin-fixed human anal tissues *ex vivo* in a similar manner to the bench sLSM device. Differences in morphologic features between normal squamous epithelium, LSIL, and HSIL were clearly visualized by the compact sLSM device. The preliminary results indicate that the compact sLSM probe might be promising for imaging epithelial cellular features in unstained human tissues *ex vivo* in a pathology lab or for directly imaging human patients *in vivo*.

Formalin-fixed anal tissues provided a negative nuclear contrast (nuclei were dark). This is contrary to fresh anal biopsy tissues stained with low-concentration acetic acid, where sLSM images exhibited bright cell nuclei.[18] While the negative nuclear contrast made sLSM imaging of fixed tissues more challenging than fresh tissues, fixed tissues were used for comparing the compact sLSM probe to the bench sLSM device, because the cellular features were fixed and did not degrade over time.

Several limitations were found in the compact sLSM probe. The measured resolution of the custom objective lens was slightly worse than the theoretical one. This discrepancy was mainly caused by the manufacturing and alignment errors. In addition, there was a difference between the PSF FWHM of the custom objective lens alone (1.65 to 1.97 $\mu$m) and the LSF FWHM of the whole probe (1.90 $\mu$m). Broadening of the LSF might have been caused by the side lobes in the objective lens PSF. Further desensitization of the objective lens during the design process and more accurate alignment might reduce the measured PSF FWHM and reduce the side lobes.

Over the imaging depth of 100 to 200 $\mu$m, cellular features were readily visible. While this imaging depth is significantly smaller than the imaging depth of OCT, it is likely adequate for visualizing nuclear changes associated with squamous intraepithelial lesions, as shown in the sLSM images of the fixed anal tissues in this paper, the sLSM images of fresh anal biopsy tissues,[18] and confocal microscopy images of cervical squamous intraepithelial lesions.[28,29] However, tissue structures in deeper tissue regions such as tumor nests might be helpful in determining the tumor invasion. In a future sLSM probe, a longer wavelength can be coupled into the illumination fiber along with 638 nm used in this paper to provide a larger imaging depth albeit the reduced resolution.[16]

In sLSM, the side-scattered light at the 90 deg angle relative to the illumination beam is detected. This is unlike most of the *in vivo* microscopy approaches (e.g., RCM), where reflected or back-scattered light is detected. While back-scattered light can be more sensitive to sub-cellular details than side-scattered light, we did not observe significant differences in visualizing nuclei in various animal and huma epithelial tissues between sLSM and RCM. However, more experiments are needed to rigorously evaluate the imaging performance difference between sLSM and RCM.

Another difference of sLSM when compared to RCM is cross-sectional imaging. In a reader study asking pathologists to make diagnosis based on sLSM images of anal biopsies, we found that the cross-sectional nature of sLSM images made the image interpretation easy. However, there will be applications where *en face* images are preferred. A stack of sLSM images can be acquired from multiple cross sections while translating the tissue with a motorized stage, and the image stack can be resliced to generate *en face* images.[30] While this approach might not be suitable for *in vivo* human subject imaging, it might serve as a good platform for comparing *en face* images between sLSM and RCM.

The image contrast was slightly degraded in the imaged obtained with the compact sLSM probe when compared with those obtained with the bench sLSM device. The contrast degradation might have been caused by stray light. Although we used a stainless-steel washer in the custom objective lens to block the stray light, there were two limitations: the washer did not completely cover the distal flange of the bi-concave lens due to the size error of the washer, and the washer was not blackened and was highly reflective. An example showing the stray light issue is the bright signals observed on the lines at group 4, element 2 of the USAF target image [Fig. 5(a)]. More careful control of stray light during the design process and use of better light-blocking material for the washer might mitigate this issue in future development.

The current sLSM probe size might be adequate for imaging excised tissues in surgical suites and pathology labs or imaging anal tissues *in vivo* when the anal canal is dilated with a rectal speculum (opening diameter = ~50 mm). However, the size of probe would need to be further miniaturized for other clinical applications such as imaging of anal mucosa through an anoscope (a hollow plastic tube with the opening diameter of 15 mm). The size of the current sLSM probe was mainly limited by the size of the CMOS sensor. By replacing the current sensor with a sensor in more compact packaging, the dimension of the probe can be further reduced. In addition, a custom objective lens with a similar NA but with a shorter focal length can be used to reduce the probe size, albeit the small FOV.

The current sLSM probe size is adequate for imaging skin, especially at anatomically hidden locations. We previously evaluated sLSM for imaging cellular structures of human skin.[30] While certain cellular structures of the skin such as keratinocytes were visible in sLSM images, the image contrast and resolution were lower than those of RCM probably because skin surface folds and index mismatching between the immersion medium and stratum corneum (refractive index = 1.5) caused significant aberrations. Further optimization of the imaging condition (e.g., using a half ball lens and immersion medium with the index of 1.5 on top of the skin surface) will be needed to improve the skin imaging performance.

The compact sLSM probe in this paper was evaluated to capture scattering signals. However, there are no fundamental limitations in using the compact sLSM probe for fluorescence imaging. It would be of interest to implement an illumination scheme of using two different spectral bands (one for fluorescence excitation and the other for scattering) and an emission filter in the detection optics, which could provide both fluorescence and scattering images with a compact LSM probe.

## Disclosures

The University of Arizona has a technology-licensing agreement with ArgosMD on the portable confocal microscopy technology. D.K. has the rights to receive royalties because of this licensing agreement. D.K. serves as a scientific advisor to ArgosMD.

## Code and Data Availability

The data underlying the results presented in this paper are not publicly available at this time but may be obtained from the authors upon reasonable request.

## Acknowledgments

The research presented was supported by the National Institute of Biomedical Imaging and Bioengineering of the National Institutes of Health (R21EB030079). The content is solely the responsibility of the authors and does not necessarily represent the official views of the National Institutes of Health.

## References

1. W. A. Wells et al., "*In vivo* and *ex vivo* microscopy: moving toward the integration of optical imaging technologies into pathology practice," *Arch. Pathol. Lab. Med.* **143**(3), 288–298 (2018).
2. K. W. Bishop et al., "*In vivo* microscopy as an adjunctive tool to guide detection, diagnosis, and treatment," *J. Biomed. Opt.* **27**(4), 040601 (2022).

3. Y. Wang et al., “Application of optical coherence tomography in clinical diagnosis,” *J. X-Ray. Sci. Technol.* **27**, 995–1006 (2019).
4. E. Cinotti et al., “Quantification of capillary blood cell flow using reflectance confocal microscopy,” *Ski. Res. Technol.* **20**(3), 373–378 (2014).
5. L. E. Meyer et al., “*In vivo* confocal scanning laser microscopy: comparison of the reflectance and fluorescence mode by imaging human skin,” *J. Biomed. Opt.* **11**(4), 044012 (2006).
6. R. A. Leitgeb, “En face optical coherence tomography: a technology review [Invited],” *Biomed. Opt. Express* **10**(5), 2177–2201 (2019).
7. J. Welzel, “Optical coherence tomography in dermatology: a review,” *Ski. Res. Technol.* **7**(1), 1–9 (2001).
8. L. Liu et al., “Imaging the subcellular structure of human coronary atherosclerosis using micro–optical coherence tomography,” *Nat. Med.* **17**(8), 1010–1014 (2011).
9. A. Dubois et al., “Line-field confocal optical coherence tomography for high-resolution noninvasive imaging of skin tumors,” *J. Biomed. Opt.* **23**(10), 106007 (2018).
10. P. J. Keller and E. H. K. Stelzer, “Quantitative *in vivo* imaging of entire embryos with digital scanned laser light sheet fluorescence microscopy,” *Curr. Opin. Neurobiol.* **18**(6), 624–632 (2008).
11. P. J. Keller and M. B. Ahrens, “Visualizing whole-brain activity and development at the single-cell level using light-sheet microscopy,” *Neuron* **85**(3), 462–483 (2015).
12. K. B. Patel et al., “High-speed light-sheet microscopy for the *in-situ* acquisition of volumetric histological images of living tissue,” *Nat. Biomed. Eng.* **6**(5), 569–583 (2022).
13. O. E. Olarte et al., “Light-sheet microscopy: a tutorial,” *Adv. Opt. Photonics* **10**(1), 111–179 (2018).
14. A. K. Glaser et al., “Light-sheet microscopy for slide-free non-destructive pathology of large clinical specimens,” *Nat. Biomed. Eng.* **1**(7), 84 (2017).
15. C. D. Nguyen et al., “Scattering-based light-sheet microscopy for rapid cellular imaging of fresh tissue,” *Lasers Surg. Med.* **53**(6), 872–879 (2021).
16. J. Zhao et al., “Investigation of different wavelengths for scattering-based light sheet microscopy,” *Biomed. Opt. Express* **13**(7), 3882–3892 (2022).
17. J. Zhao et al., “Speckle and shadow artifacts reduction in scattering-based light sheet microscopy,” in *Biophotonics Congr.: Opt. in the Life Sci. 2023 (OMA, NTM, BODA, OMP, BRAIN)*, Optica Publishing Group, Vancouver, British Columbia, p. DTu2A.3 (2023).
18. B. Liang et al., “Scattering-based light sheet microscopy imaging of fresh anoscopic biopsy specimens: a prospective descriptive study characterizing anal lesionsitle,” in *Int. Anal. Neoplasia Soc. 2023 Sci. Meet* (2023).
19. A. R. Rouse et al., “Design and demonstration of a miniature catheter for a confocal microendoscope,” *Appl. Opt.* **43**(31), 5763–5771 (2004).
20. M. Zaman and Y. Büyükalp, “Design of a high numerical aperture achromatic objective lens for endomicroscopy,” *Opt. Eng.* **58**, 075101 (2019).
21. K. Carlson et al., “*In vivo* fiber-optic confocal reflectance microscope with an injection-molded plastic miniature objective lens,” *Appl. Opt.* **44**(10), 1792–1797 (2005).
22. S. Pacheco et al., “High resolution, high speed, long working distance, large field of view confocal fluorescence microscope,” *Sci. Rep.* **7**(1), 13349 (2017).
23. B. Liang et al., “Scattering-based light-sheet microscopy imaging of human papillomavirus-associated squamous lesions of the anal canal: a proof-of-principle study,” *Mod. Pathol.* **37**(6), 100493 (2024).
24. M. Matiatou et al., “Data on the refractive index of freshly-excised human tissues in the visible and near-infrared spectral range,” *Results Phys.* **22**, 103833 (2021).
25. M. Kruczkowski et al., “Predictions of cervical cancer identification by photonic method combined with machine learning,” *Sci. Rep.* **12**(1), 3762 (2022).
26. P. Zhou, “Tutorial of tolerancing analysis using commercial optical software,” in *OPTI* (2006).
27. P. Ricci et al., “Removing striping artifacts in light-sheet fluorescence microscopy: a review,” *Prog. Biophys. Mol. Biol.* **168**, 52–65 (2022).
28. T. Collier et al., “Real-time reflectance confocal microscopy: comparison of two-dimensional images and three-dimensional image stacks for detection of cervical precancer,” *J. Biomed. Opt.* **12**(2), 024021 (2007).
29. F. Sheikhzadeh et al., “Quantification of confocal fluorescence microscopy for the detection of cervical intraepithelial neoplasia,” *Biomed. Eng. Online* **14**(1), 96 (2015).
30. C. D. Nguyen, *Light Sheet Reflectance Microscopy*, The University of Arizona (2019).

**Jingwei Zhao** is a PhD candidate at the University of Arizona. She received her BS degree in photoelectric information science and engineering from the School of Physics at the University of Science and Technology of China in 2018, and her MS degree in optical sciences from Wyant College of Optical Sciences at the University of Arizona in 2022. She is interested in the design and development of medical imaging devices and medical image processing. She is a student member of SPIE.

**Yongjun Kim** is an MS student in biomedical engineering at the University of Arizona, focusing on advanced medical imaging techniques. He received his BS degree in biotechnology from South Dakota State University in 2019. He is interested in the development of medical imaging devices and algorithms for enhanced disease diagnosis. He is a student member of SPIE.

**Momoka Sugimura** is a PhD student at Wyant College of Optical Sciences at the University of Arizona. She received her BS degree in optical sciences and engineering from the same institution in 2020. Her PhD research focuses on developing low-cost, portable, and high-speed reflectance confocal microscopy for *in vivo* tissue imaging. She is a student member of SPIE.

**Kenneth Marcelino** is a PhD student at the University of Arizona. She received her BS degree in physics from the College of Arts and Sciences at Loyola University Maryland in 2021. She works in the translational optical imaging lab in the University of Arizona and is interested in medical imaging device development. She is a student member of SPIE.

**Rafael Romero** is a PhD student in biomedical engineering at the University of Arizona. He received his BS and MS degrees in biomedical engineering from the same institution in 2021 and 2023. His PhD research focuses on developing low-cost, portable, cross-polarized microscopy for *in vivo* skin imaging.

**Brooke Liang** is a gynecologic pathology fellow at Stanford University School of Medicine. She completed her residency training in anatomic and clinical pathology at the University of Chicago and Stanford University. She received her MD and MA degrees from Washington University in St. Louis School of Medicine.

**Michelle Khan** is a board-certified obstetrician gynecologist with training in reproductive infectious diseases. She completed medical school at Rutgers University—Robert Wood Johnson Medical School, residency in Gynecology/Obstetrics at the Johns Hopkins Hospital, and fellowship in Reproductive Infectious Diseases at the University of California San Francisco. Her clinical expertise is in screening, evaluation and treatment of HPV-related diseases and prevention of HPV-related cancers.

**Eric Yang** is a clinical associate professor of pathology at Stanford University School of Medicine. He completed residency and fellowship trainings at Brigham and Women's Hospital, Harvard Medical School in Anatomic Pathology, Women's and Perinatal Pathology, and Cytopathology. He received his MD and PhD degrees from Tufts University School of Medicine. His research focuses on novel pathology-based technology (*in vivo* microscopy, digital pathology, and AI-applications) for the advancement of cancer diagnosis and screening.

**Dongkyun Kang** is an associate professor of optical sciences and biomedical engineering at the University of Arizona. He received his PhD in mechanical engineering from Korea Advanced Institute of Science and Technology in 2006. Before joining the University of Arizona in 2017, he worked as an assistant professor of dermatology at the Harvard Medical School and Massachusetts General Hospital. His Translational Optical Imaging Lab develops low-cost, *in vivo* microscopy tools for disease diagnosis in low-resource settings. He is a senior member of SPIE.